The Astrophysical Journal, 829:65 (16pp), 2016 October 1 doi:10.3847/0004-637X/829/2/65

PANCHROMATIC IMAGING OF A TRANSITIONAL DISK: THE DISK OF GM AUR IN OPTICAL AND FUV SCATTERED LIGHT

J. B. Hornbeck[1], J. R. Swearingen[2], C. A. Grady[3,4], G. M. Williger[1,5,6,7], A. Brown[8], M. L. Sitko[2,9], J. P. Wisniewski[10], M. D. Perrin[11], J. T. Lauroesch[1], G. Schneider[11], D. Apai[12,13], S. Brittain[14], J. M. Brown[15], E. H. Champney[2], K. Hamaguchi[16,17], Th. Henning[18], D. K. Lynch[19], R. Petre[20], R. W. Russell[19], F. M. Walter[21], and B. Woodgate[20,22]

[1] Department of Physics & Astronomy, University of Louisville, Louisville, KY 40292, USA; jeremy.hornbeck@louisville.edu, gmwill06@louisville.edu
[2] Department of Physics, University of Cincinnati, 400 Geology/Physics Building, P.O. Box 210011, Cincinnati, OH 45221-0377, USA
[3] Eureka Scientific, 2452 Delmer Street, Suite 100, Oakland, CA 96402, USA; carol.a.grady@nasa.gov
[4] Exoplanets and Stellar Astrophysics Laboratory, Code 667, Goddard Space Flight Center, Greenbelt, MD 20771, USA
[5] Laboratoire Lagrange, Université de Nice, UMR 7293, F-06108 Nice Cedex 2, France
[6] IACS, Dept. of Physics, Catholic University of America, Washington DC 20064, USA
[7] Jeremiah Horrocks Inst., U Central Lancashire, Preston PR1 2HE, UK
[8] CASA, University of Colorado, Boulder, CO 80309-0593, USA
[9] Center for Extrasolar Planetary Systems, Space Science Institute, Boulder, CO 80301, USA
[10] Homer L. Dodge Department of Physics & Astronomy, University of Oklahoma, 440 W. Brooks Street, Norman, OK 73019, USA
[11] Space Telescope Science Institute, 3700 San Martin Drive, Baltimore, MD 21218, USA
[12] Department of Astronomy and Steward Observatory, University of Arizona, 933 N. Cherry Avenue, Tucson, AZ 85721, USA
[13] Department of Planetary Sciences and Lunar and Planetary Laboratory, University of Arizona, 1629 E. University Boulevard, Tucson, AZ 85721-0092, USA
[14] Department of Physics & Astronomy, Clemson University, 118 Kinard Laboratory, Clemson, SC 29634-0978, USA
[15] Harvard-Smithsonian Center for Astrophysics, 60 Garden Street, Cambridge, MA 02138, USA
[16] Department of Physics, UMBC, Baltimore, MD 21250, USA
[17] CRESST and X-ray Astrophysics Laboratory NASA/GSFC, Greenbelt, MD 20771, USA
[18] Max-Planck-Institut Für Astronomie, Königstuhl 17, D-69117 Heidelberg, Germany
[19] The Aerospace Corporation, Los Angeles, CA 90009, USA
[20] NASA's Goddard Space Flight Center, Greenbelt, MD 20771, USA
[21] Department of Physics and Astronomy, Z = 3800, Stony Brook University, Stony Brook, NY 11794-3800, USA
Received 2015 July 23; revised 2016 April 30; accepted 2016 May 3; published 2016 September 22

ABSTRACT

We have imaged GM Aurigae with the *Hubble Space Telescope*, detected its disk in scattered light at 1400 and 1650 Å, and compared these with observations at 3300 Å, 5550 Å, 1.1 μm, and 1.6 μm. The scattered light increases at shorter wavelengths. The radial surface brightness profile at 3300 Å shows no evidence of the 24 au radius cavity that has been previously observed in submillimeter observations. Comparison with dust grain opacity models indicates that the surface of the entire disk is populated with submicron grains. We have compiled a spectral energy distribution from 0.1 μm to 1 mm and used it to constrain a model of the star + disk system that includes the submillimeter cavity using the Monte Carlo radiative transfer code by Barbara Whitney. The best-fit model image indicates that the cavity should be detectable in the F330W bandpass if the cavity has been cleared of both large and small dust grains, but we do not detect it. The lack of an observed cavity can be explained by the presence of submicron grains interior to the submillimeter cavity wall. We suggest one explanation for this that could be due to a planet of mass $<9\,M_J$ interior to 24 au. A unique cylindrical structure is detected in the far-UV data from the Advanced Camera for Surveys/Solar Blind Channel. It is aligned along the system semiminor axis, but does not resemble an accretion-driven jet. The structure is limb brightened and extends 190 ± 35 au above the disk midplane. The inner radius of the limb brightening is 40 ± 10 au, just beyond the submillimeter cavity wall.

Key words: circumstellar matter – protoplanetary disks – stars: individual (GM Aur) – stars: protostars – stars: variables: T Tauri, Herbig Ae/Be – ultraviolet: planetary systems

1. INTRODUCTION

Transitional disks are protoplanetary disks that are in the process of evolving from a gas-rich primordial disk to a gas-poor debris disk. During this transition period, material in the disk within the first few tens of astronomical units (au) from the star clears to form an optically thin gap or cavity. Consistent with the presence of accretion, these objects retain an inner disk within a few au of the star (Hartigan et al. 1990). If the cleared cavities were devoid of material, these systems would be unable to replenish their inner disk and accretion would cease relatively quickly. Many of these objects continue to accrete material while having cavities tens of au in radii, as evidenced by mid-IR/submillimeter/millimeter observations (Lubow & D'Angelo 2006; Rice et al. 2006; Salyk et al. 2013).

One possible explanation for such cavity generation is a filtration mechanism that allows only small dust grains, which would be undetected in the submillimeter/millimeter data, to migrate inward through the gap entrained with the still-accreting gas from the outer disk (Quillen et al. 2004). Cieza et al. (2012) compared several processes driving disk evolution, including grain growth, the effect of planets, and photoevaporation mechanisms. Starting with the hypothesis that small grains in a cavity are part of the process of grain growth, they found that grain growth can account for >40% of transition disks around K- and M-type stars, though the process can have complicating factors like fragmentation or replenishment

[22] Deceased.

Table 1
HST Filter Characteristics

Filter	Wavelengths (Å)	Plate Scale	Angular Resolution 80% Encircled Energy
F140LP	1360–1580 50% max transmission	$0.034 \times 0\farcs030$	$0\farcs30$ (based on F150LP)
F165LP	1640–1830 50% max transmission	$0.034 \times 0\farcs030$	$0\farcs30$ (based on F150LP)
F330W	$\lambda_{\rm eff} = 3376$, $\Delta\lambda = 529$	$0.028 \times 0\farcs025$	$0\farcs25$ (based on F220W)
F555W	$\lambda_{\rm pivot} = 5439$, $\Delta\lambda = 1236$	$0.046 \times 0\farcs046$	$0\farcs15$

(Dullemond & Dominik 2005). The dust grains that make up the interstellar medium (ISM) are estimated to include a range in size from 0.005 to 1 μm (Mathis et al. 1977). Rice et al. (2006) suggest that filtration of small ISM-like grains into the cavity devoid of larger grains could be an indication that a planet with a mass of 1–6 M_J resides within the cavity. Simulations by Zhu et al. (2012) and de Juan Ovelar et al. (2013) produce similar results, and they also suggest the presence of one or more gas giant planets as a disk-clearing mechanism. Far-UV (FUV) driven neutral atomic or molecular disk winds have also been considered as a possible mechanism for disk dispersal. At large radii, giant planets have difficulty clearing material on a sufficiently short timescale to be consistent with estimates of the disk-dispersal time for T Tauri stars ($\approx 10^5$ yr; Simon & Prato 1995; Wolk & Walter 1996). In rich cluster environments, Johnstone et al. (1998) showed that FUV radiation from nearby stars can dominate the photo-evaporation rate. This, however, does not explain the rapid dispersal of disks around young stars with no nearby source of the FUV flux. Gorti & Hollenbach (2009) have considered flows driven by FUV radiation from the central star and argued that mass-loss rates of the order of $10^{-8}\,M_\odot$ yr^{-1} can be obtained at large radii (>100 au).

Mapping the dust grain size distribution throughout the disk can indicate which mechanism is responsible for clearing material from the disk. Dust grains scatter light most efficiently at wavelengths comparable to their size, so determining whether submicron dust grains are present inside a disk cavity requires observations to be in submicron bandpasses. Disks with large cavities provide test beds for multiwavelength observations probing the surface of the disk to analyze the light-scattering properties and size distribution of the dust grains. This method for determining grain properties and distributions has been employed successfully at submillimeter and longer wavelengths (Banzatti et al. 2011; Pérez et al. 2012), but relies on scattered light rather than thermal emission. High-contrast FUV and optical images have the added benefit of a smaller inner working angle (IWA) than at longer wavelengths with the same instrument. For disks with cavities tens of au in diameter, such observations allow us to map the spatial distribution of gas and small (submicron) grain reflection nebulosity present at the disk surface, both interior and exterior to the cavity wall. If small-grain dust exists interior to the large grain cavity wall, we would not expect transitional disks with relatively high accretion rates to have an optically thin cavity at short (FUV and optical) wavelengths.

The disk associated with the classical T Tauri star GM Aur (K5.5 $\pm$ 1.0, $B - V = 1.12$; Espaillat et al. 2010) has been studied extensively for 2 decades with the *Hubble Space Telescope* (*HST*). The distance to GM Aur is 136^{+50}_{-29} pc (Bertout & Genova 2006), and the inclination from pole-on for its disk is 55° (Calvet et al. 2005; Hughes et al. 2009; Andrews et al. 2011). The disk has been detected in scattered optical and near-IR (NIR) light (Stapelfeldt et al. 1995; Schneider et al. 2003). The disk became categorized as transitional when millimeter and submillimeter observations detected a cleared inner cavity extending from the star to between 20 and 28 au (Calvet et al. 2005; Hughes et al. 2009; Andrews et al. 2011; Gräfe et al. 2011); in this paper we assume that the submillimeter cavity is 24 au in radius. GM Aur is also accreting material at a rate of $\approx 10^{-8}\,M_\odot$ yr^{-1} (Gullbring et al. 1998; White & Ghez 2001; Ingleby et al. 2015), suggesting that material is migrating inward from the outer disk, through the submillimeter cavity, and accreting onto the star. This can be directly tested with FUV and short-wavelength optical observations. We have acquired the requisite data sets with *HST*'s Advanced Camera for Surveys (ACS) using the Solar Blind Channel (SBC), as well as archival data from both the High Resolution Channel (HRC) and the second-generation Wide Field Planetary Camera (WFPC2).

In this paper *HST* data of GM Aur, along with data from a wide variety of other instruments, are used to create a spectral energy distribution (SED), all of which we then use to model the GM Aur star+disk system. We probe material within the submillimeter cavity region, to test the hypothesis that small-grain dust exists within the 24 au cavity of GM Aur's transitional disk. A description of the data used and the data reduction are described in Section 2. Our analysis and results are found in Section 3, with a discussion in Section 4.

2. OBSERVATIONS AND DATA REDUCTION

GM Aurigae has been observed by *HST* at multiple epochs over wavelengths ranging from the FUV to NIR, and at longer wavelengths by other instruments. The NIR observations obtained by the Near Infrared Camera and Multi-Object Spectrometer (NICMOS) were analyzed and discussed in Schneider et al. (2003). The *HST* WFPC2 F555W, ACS/HRC F330W, and ACS/SBC F140LP and F165LP data sets have not previously been addressed in detail and so are presented here. The central wavelengths, bandpasses (FWHMs), spatial sampling, and angular resolution from Maybhate & Armstrong (2010) and McMaster et al. (2008) are summarized in Table 1. The longer-wavelength WFPC2 data were taken with very short and 20 times deeper exposures such that the short exposures were underexposed, while the longer exposures were highly saturated. We have therefore excluded them from our analysis. One of our goals is to examine the surface brightness profile as close to the edge of the submillimeter cavity as possible. We can do this with the F555W and shorter-wavelength observations. Our goals also include estimating the effects of (i) random errors in the scatter from multiple observations of GM Aur and a given point-spread function (PSF) template star (possible for F555W observations) and (ii) systematic errors arising from the choice of one PSF template

Table 2
HST Observations

Object	Data Set	Program ID	Date	Instrument	Filter	Exp (s)
GM Aur	JA5M01020-30	11336	2008 Aug 13	ACS/SBC	F140LP	2520,2552
GM Aur	JA5M01010	11336	2008 Aug 13	ACS/SBC	F165LP	2528
GM Aur	J8MS09PNQ	9812	2003 Dec 31	ACS/HRC	F330W	360
GM Aur	U2RD0401T-04T	6223	1995 Jul 29	WFPC2/PC1	F555W	4 × 30
			PSF Template Observations			
NQ UMa	JBDF07010	12016	2010 Jun 05	ACS/SBC	F140LP	2648
NQ UMa	JBDF06010	12016	2010 Jun 03	ACS/SBC	F165LP	2648
HD 202560	J8HV03031	9655	2002 Dec 13	ACS/HRC	F330W	2 × 2
CY Tau	J8MSA1MUQ	9812	2003 Dec 27	ACS/HRC	F330W	360
DS Tau	J8MS08HEQ	9812	2003 Dec 30	ACS/HRC	F330W	360
HD 283572	U2RD0301T-04T	6223	1995 Jul 23	WFPC2/PC1	F555W	4 × 1.6
			STIS Observations			
GM Aur	OB3R04050	11608	2011 Sep 11	STIS	G140L	3020
GM Aur	OB3R04040	11608	2011 Sep 11	STIS	G230L	1231
GM Aur	OB3R04010	11608	2011 Sep 11	STIS	G430L	35
GM Aur	OB3R04020	11608	2011 Sep 11	STIS	G750L	8

star versus another (done for F330W observations). A detailed list of the *HST* observations we have used is in Table 2.

2.1. WFPC2 Broadband Optical Data—F555W

GM Aur was observed as a suite of 4 × 30 s exposures with WFPC2 and the F555W filter, using a 4 pt, 20 pixel (0.″91) dither pattern on the PC1 chip (PI Trauger). The WFPC2 data were processed and reduced with the On-The-Fly Reprocessing (OTFR) pipeline, yielding four flat-fielded individual (undrizzled) images prior to our analysis (Gonzaga et al. 2010). Our starting point for the data reduction was the pipeline-processed science image (c0m.fits) file set, which retains the full sampling of the planetary camera chip data. The disk is detected in the raw data at each dither position, but the disk/star contrast can be improved by subtraction of suitably scaled and registered PSF template data. We checked the MAST archive for a suitably exposed PSF template star for this WFPC2/PC1 configuration. Three template stars were considered: the white dwarf HIP 66578 (Gianninas et al. 2011), the sdF star HIP 109558, and the G5IV star HD 283572. The data for HIP 66578 and HIP 109558 were obtained for photometric calibration of WFPC2, but were shallow exposures that do not map the wings of the stellar PSF much beyond the first Airy ring. As a result, we have made use of the data for HD 283572 (G5IV, $B - V = 0.77$; Strassmeier 2009).[23] HD 283572 was observed as part of the same program (HST-GTO-6223) and has data with the same relative exposure depth and dither pattern as for GM Aur. Both data sets are slightly overexposed and show some bleeding of charge in the detector $+y$ direction over ±2–3 pixels. The HD 283572 and GM Aur images were taken close in time (6 days apart), space (7.°6 apart on the sky), and orientation (4.°3 difference in orientation angle). We did not find any other satisfactory PSF star.

We constructed 16 target-PSF template image pairs. These image pairs were registered to the first of the GM Aur observations, and then we calculated a median (to eliminate cosmic rays/bad pixels) and a standard deviation image using the IDL routine Image Display Paradigm #3 (IDP3; Lytle et al. 1999; Schneider & Stobie 2002). Manual PSF subtraction using a method nearly identical to this was described by Krist et al. (2000), doing the photometry by "counting the number of saturated pixels and converting to fluxes assuming a full-well electron depth, as described by Gilliland (1994). These values were then multiplied by a factor of 1.10 to account for flux outside of the saturated regions (determined by masking out the same pixels in simulated PSFs)." Krist et al. (2000) note that their method of estimating fluxes in the case of using saturated pixels is good to ∼5%. Diffraction spike residuals are visible in the median image, as expected for image sets where there are changes in *HST* focus after slews ("breathing") and where the color match between the PSF template and the target is imperfect. We then computed median and standard deviation images for the GM Aur–GM Aur data and for PSF–PSF and find similar residuals and variability *for both stars*, consistent with detection of stellar activity and/or accretion luminosity variations. Variation in the residual diffraction spikes was seen between image pairs, at a level consistent with *HST* thermally driven focus changes and stellar activity in the raw data, for *both* GM Aur and the PSF template object HD 283572. Each of the 16 GM Aur–HD 283572 image pairs is shown in Figure 1 to illustrate the variation between exposures. We also tested the variation between individual exposures by subtracting exposures of each object from a different exposure of itself (Figure 2). The mean and standard deviation of the rms values around the disk (within 1.″2 of GM Aur) for the GM Aur—PSF subtractions are 3.1 ± 2.0 counts sampled in four widely separated test regions avoiding diffraction spikes and containing between 40 and 138 pixels each. For the GM Aur–GM Aur images for two different exposures the rms values are 0.9 ± 0.1 counts in the same four test regions, while for a pair of PSF–PSF images they are 1.1 ± 0.3. Farther away, about 4″ from the flux centroid, the rms values for GM Aur–PSF are 0.6 ± 0.1 for four larger background test regions containing 900–2800 pixels each. The GM Aur–GM Aur values are 0.5 ± 0.1, while for the PSF–PSF subtraction they are 0.8 ± 0.1. We conclude that the individual exposure variations contribute on the order of one-third of the noise level

[23] The original reference to HD 283572 is Walter et al. (1987), who found a slightly redder value of $B - V = 0.83$.

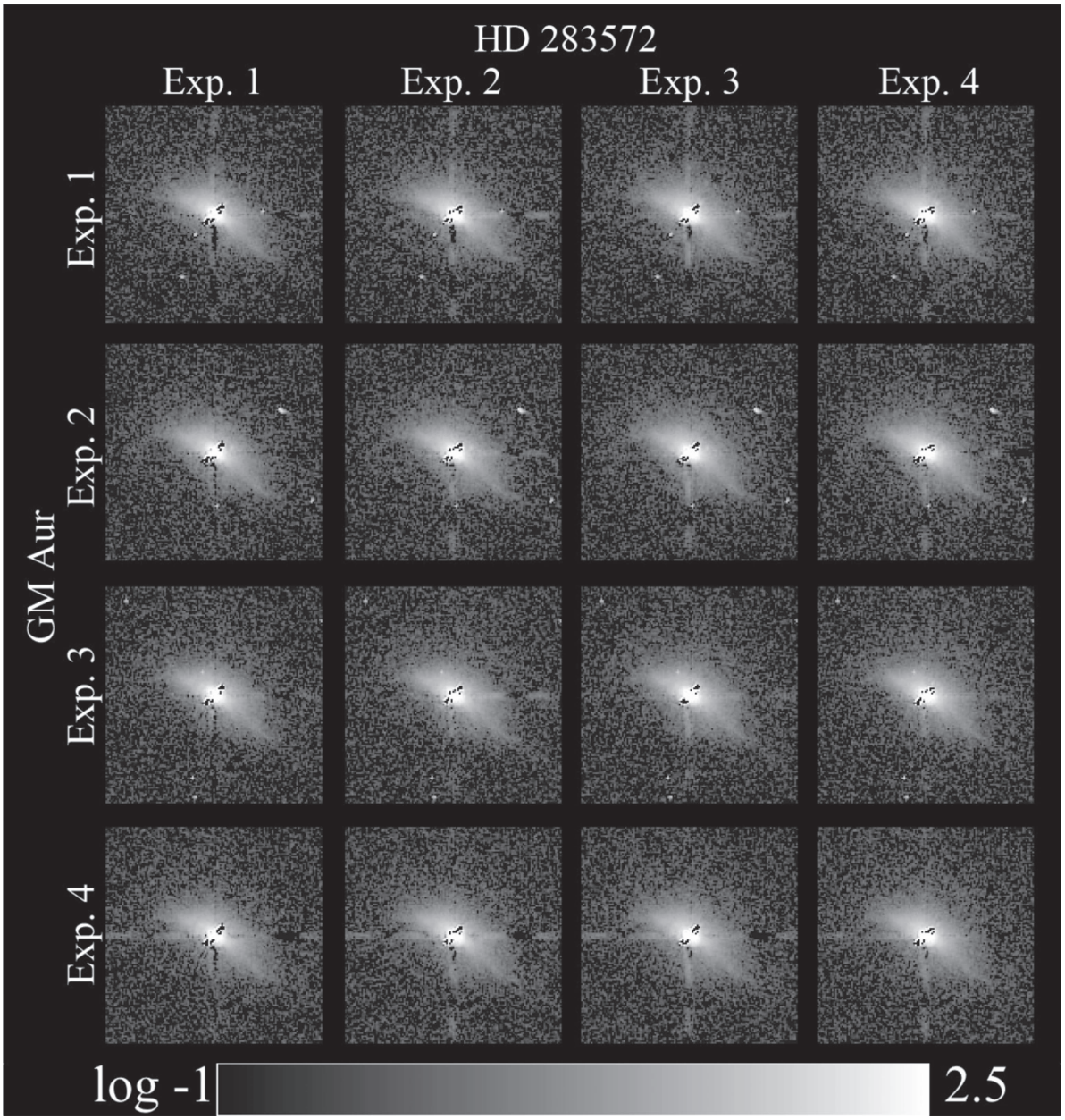

Figure 1. Four exposures of GM Aur in the F555W filter subtracted from each of the four exposures of HD 283572. We attribute the variation between exposures to environmental stresses on the spacecraft while in orbit. Images have been rotated to show N up and E to the left. The combination of GM Aur exposure 3 and HD 283572 exposure 4 was used for illustration in Figure 4.

compared to a single GM Aur frame with a single PSF frame subtracted from it.

To further characterize the uncertainty arising from individual GM Aur and HD 283572 exposures, the standard deviation for each pixel was calculated based on each of the 16 subtraction pairs. Simple photometry with a 13×7 pixel rectangular aperture for GM Aur shows a flux variation of 0.3% between the exposures, while a 16×7 rectangular aperture for HD 283572 reveals variations of up to 2.8% between exposures, with the third exposure having the highest flux. These variations are less than the 5% quoted accuracy for photometry based on counting saturated pixels (Krist et al. 2000). We frequently could null two of the diffraction spikes satisfactorily, but could not simultaneously null all four diffraction spikes completely for any of the 16 exposure-subtraction combinations. The variations in nulling efficiency show a spread of scale factors on the order of 25%–30%. These variations dominate over other sources of uncertainty when determining the disk-scattering fraction ($F_{\rm disk}/F_{\rm star}$). Although there is only one suitable PSF template available in the *HST* archive for F555W, we estimate the uncertainty from PSF template selection to be similar to that derived for F330W, on the order of ~25% (see below).

2.2. HRC Optical Data—F330W

For our analysis, we use the pipeline-processed, calibrated flat-fielded (flt) files for the one 360 s F330W exposure employed for GM Aur (PI Hartigan). We checked the MAST archive for a suitably exposed star to act as a satisfactory PSF template, and we identified HIP 66578, HIP 109558,

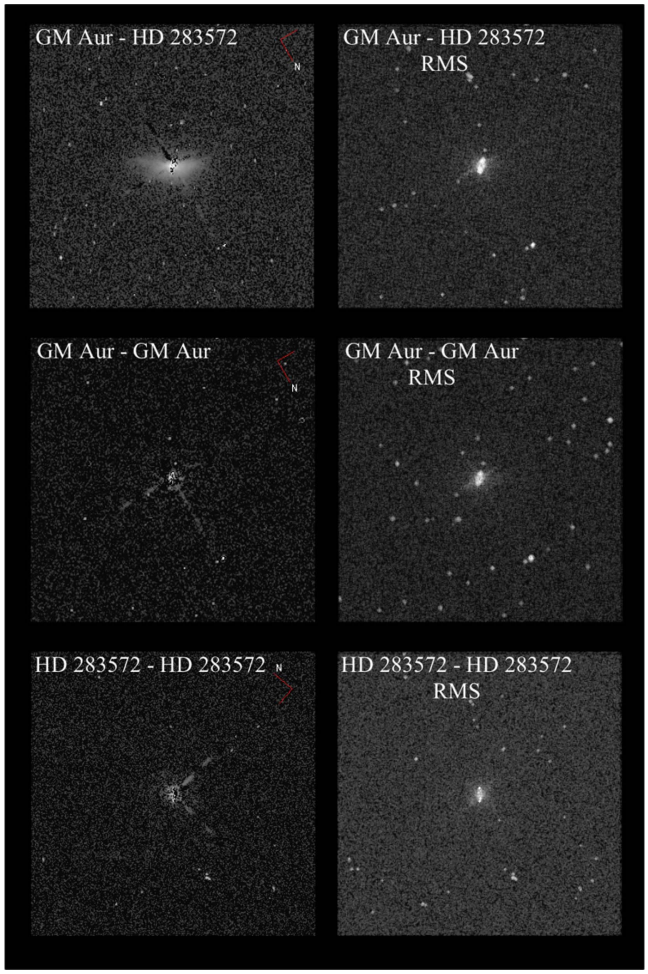

Figure 2. To determine the significance of variations between individual exposures, we compared an rms image of the PSF-subtracted data for GM Aur–HD 283572 with subtractions of GM Aur from itself and HD 283572 from itself. Unsurprisingly, the pixel-to-pixel variations are smallest for the self-subtracted images. See the text for values.

HD 202560 (AX Mic), CY Tau, and DS Tau as possible candidates for this ACS/HRC configuration.

As with the F555W data, we scaled each of the PSF templates to optimally null the diffraction spikes. We varied the scale factor so that the profile of the residual diffraction spike was within $\leqslant \pm 1\sigma$ from the local mean, determined from local rms variations in the data. This gave the bounds for the uncertainty in the scale factor and at the same time nulled any tiger-striping/Airy ring residuals. We compared each of the PSF subtractions from GM Aur for each template star individually, to estimate the (systematic) uncertainty arising from PSF template selection. We similarly created a σ image for each PSF subtraction, for statistical error use with the surface brightness profile calculation. The uncertainty in the scale factor for the PSF subtraction is the dominant source of flux uncertainty in each of the PSF-subtracted images, on the order of ~25%.

The subtractions for the bluest two stars, HIP 66578 (white dwarf DA2.4) and HIP 109558 (sdF8), have Airy ring residuals, indicating color mismatches. The best color matches came from the nearby flare star HD 202560 (M0V)[24] and the classical T Tauri stars CY Tau (M1.5) and DS Tau (K4V:e, Figure 3). MAST contains a single 360 s exposure for CY Tau and DS Tau and 2 × 2 s exposures for HD 202560. We ended up using a median of the three stars for the PSF template. The variation in the PSF-subtracted disk flux minus the PSF flux is ~6%–8% for the PSF derived from the median of the three stars, versus each individual PSF template.

2.3. SBC FUV Data—F140LP and F165LP

We employ GM Aur images in the FUV with the ACS/SBC using the F140LP and F165LP filters (PI A. Brown). This observing strategy was chosen to exclude geocoronal Lyα and O I. We used the flat-fielded, uncombined/individual exposures (flt), uncorrected for geometric distortion, initially processed via the OTFR pipeline (Pavlovsky et al. 2006).

PSF subtractions are best done in the detector frame with images that have not been corrected for geometric distortion. The correction mapping will change between orientations, and the PSF primarily refers to the detector frame. The data reduction pipeline has historically concatenated the geometric distortions, which would be detrimental to PSF subtraction. Additionally, the PSF subtraction deals with scales of 1–2″, whereas the geometric distortion becomes significant on scales approaching the order of the field of view. We queried the STScI Help Desk in 2016 March and were told that the last time the geometric distortion was updated was in 2008, with no further updates currently planned.

There are not many choices available for suitable PSF templates with the F140LP and F165LP filters. We considered the white dwarf GD 71 ($B - V = -0.249$; Landolt 1992), which is likely an extreme in color match. We also examined NQ UMa (G9V, $B - V = 0.81$; Montes et al. 2001).[25] The $B - V$ color is typical of a G9V star, so we conclude that there is no significant foreground extinction. NQ UMa was observed in the FUV with the ACS/SBC (PI C. Grady) with the F140LP and F165LP filters (Hornbeck et al. 2012). Of the two, NQ UMa is the closer color match to the photosphere, so we consider it the preferred PSF template between the two. The integration time in each bandpass for NQ UMa was 2648 s. We used the analogous (flat-fielded, individual) exposures, similar to how we worked with the F555W data. Inspection of the raw data for GM Aur demonstrates that the image lacks the bright core typical of both unresolved sources (NQ UMa or GD 71). Since GD 71 has a color difference with GM Aur, the effect cannot be chromatic. In the FUV, the light from GM Aur is not dominated by an unresolved source, but rather by extended emission. For both GM Aur and NQ UMa, for presentation purposes, we binned the pixels slightly along the y-axis to produce $\approx 0\farcs034 \times 0\farcs034$ pixel^{-1}.

The PSF subtraction process for the ACS/SBC data was the same as for the longer-wavelength images, except that the nulling was done on the core of GM Aur, because no diffraction spikes were visible, indicating that $F_{\rm disk}/F_{\rm star}$ was large. The lower bound for the scale factor was taken at the point where the peak of the PSF standard matched the peak of the GM Aur central pixel flux. The upper bound was taken by requiring the flux in an inner 5 pixel radius to be matched for the PSF standard and GM Aur. We can measure flux to an inner radius of $\approx 0\farcs1$ (a 3 pixel radius).

[24] These spectral types are from simbad.u-strasbg.fr/simbad.

[25] simbad.u-strasbg.fr/simbad.

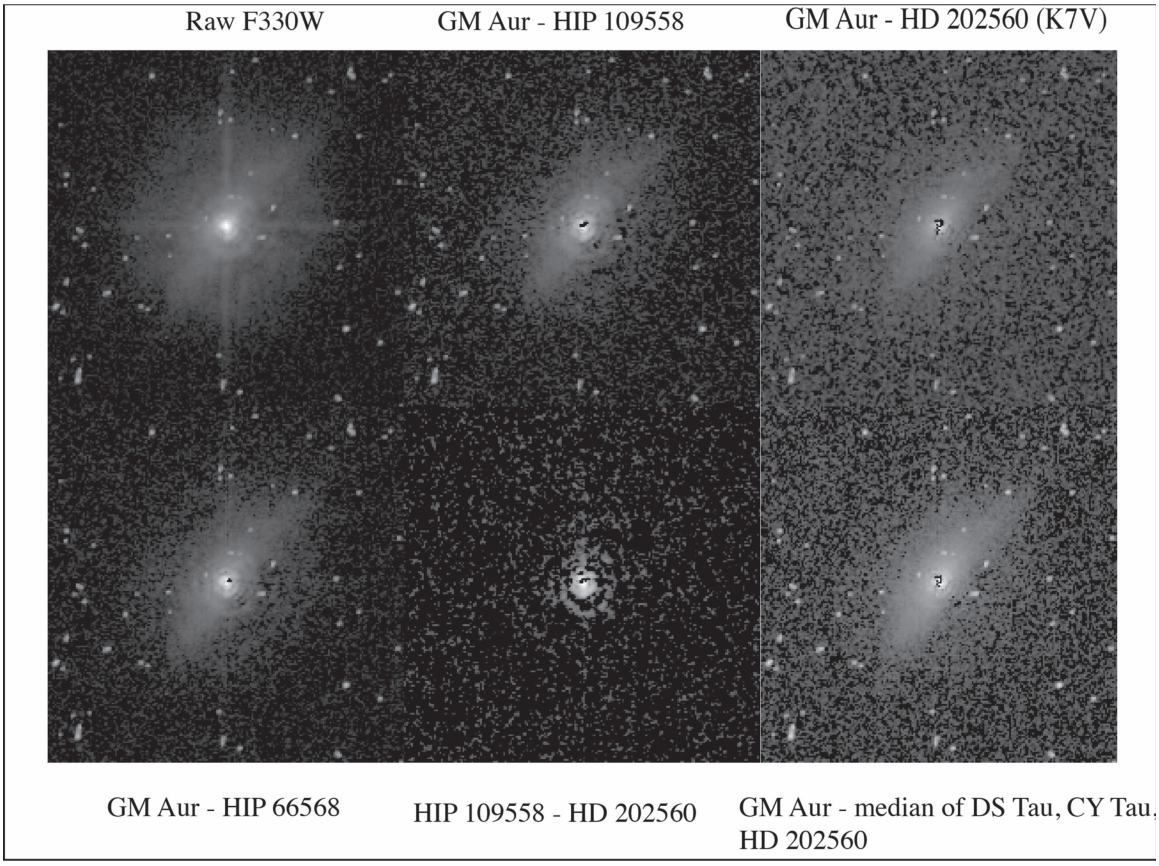

Figure 3. Example subtractions for the F330W images of GM Aur and a series of PSF standard stars. Upper left: raw image. Lower left and upper center: subtractions with HIP 66578 and HIP 109558. Lower center: HIP 109558–HD 202560, with the residual indicating a color difference. Upper and lower right: subtractions with HD 202560 and a median of HD 202560, CY Tau, and DS Tau.

2.4. Other Data

Modeling the SED of GM Aur over the widest possible wavelength range required additional data from a series of data archives and ground-based telescopes. Fortunately, a thorough collection of data across a large wavelength range exists for this purpose. The data we use provide wavelength coverage from 0.1 to 1000 μm. The FUV, near-UV, and optical spectroscopic data were obtained by STIS on 2011 September 11. Optical and NIR spectrometry was obtained with SpeX at the NASA Infrared Telescope Facility (IRTF) from 0.7 to 5.3 μm over 5 nights in 2011 September and 2012 January (Ingleby et al. 2015). The NIR photometric data points for GM Aur were obtained with the Two Micron All Sky Survey (2MASS). Our near- to mid-IR data for GM Aur come from the *Wide-Field Infrared Survey Explorer*, *Spitzer* Infrared Spectrograph (IRS), and *AKARI*/IRC data (Ishihara et al. 2010). Our mid- to far-IR data points were obtained with AKARI-FIS and *IRAS*, and additional data were supplied by the following literature: AEF90 = Adams et al. (1990), AW05 = Andrews & Williams (2005), WSD89 = Weintraub et al. (1989), and KSB93 = Koerner et al. (1993).

3. RESULTS AND ANALYSIS

3.1. High-contrast Imagery from HST

In 1.1 and 1.6 μm NICMOS imagery, Schneider et al. (2003) detected scattered light from the disk of GM Aur with a major axis along position angle PA = 58.°5 ± 2.°5 and semiminor axis in the forward-scattering direction to be PA = 328.°5 ± 2.°5, consistent with submillimeter-wavelength observations of the disk (Hughes et al. 2009). Stapelfeldt et al. (1995) detected scattered light from the disk in WFPC2 bandpasses at 5550 and 8140 Å. After PSF subtraction, we detect nebulosity in the optical (3300 Å) and FUV (1400 and 1650 Å) bandpasses (Figure 4). To verify our placement of the major axis for a radial surface brightness measurement, we constrain the disk major axis from the images in the F330W and F555W bandpasses and determined a PA of 59° ± 3°, consistent with the measurements in Schneider et al. (2003). The illuminated portion of the disk that is detected in each bandpass varies with exposure depth, so it is likely that we are not detecting signal from the full extent of the disk. However, the disk is similar in appearance in the optical bandpasses, both in and out of bands with emission lines (5550 and 3300 Å, respectively). The consistency of the geometry in the optical bandpasses indicates that what we are detecting in these bands is reflection nebulosity. The measured extent of the disk for each bandpass, as well as the aspect ratio, can be found in Table 3 and is consistent with a flared disk viewed at an inclination from pole-on of 56.°5 ± 3.°5 (Whitney & Hartmann 1992; Stark et al. 2006), which we adopt as the disk inclination for this paper. Interestingly, the geometry of the disk changes abruptly in the FUV bandpasses. An additional component to the nebulosity, aligned along PA = 150° ± 5°, is marginally detected at F165LP and firmly detected in F140LP and will be discussed in Section 3.4 in greater detail. The ACS/SBC and HRC data now extend the scattered-light

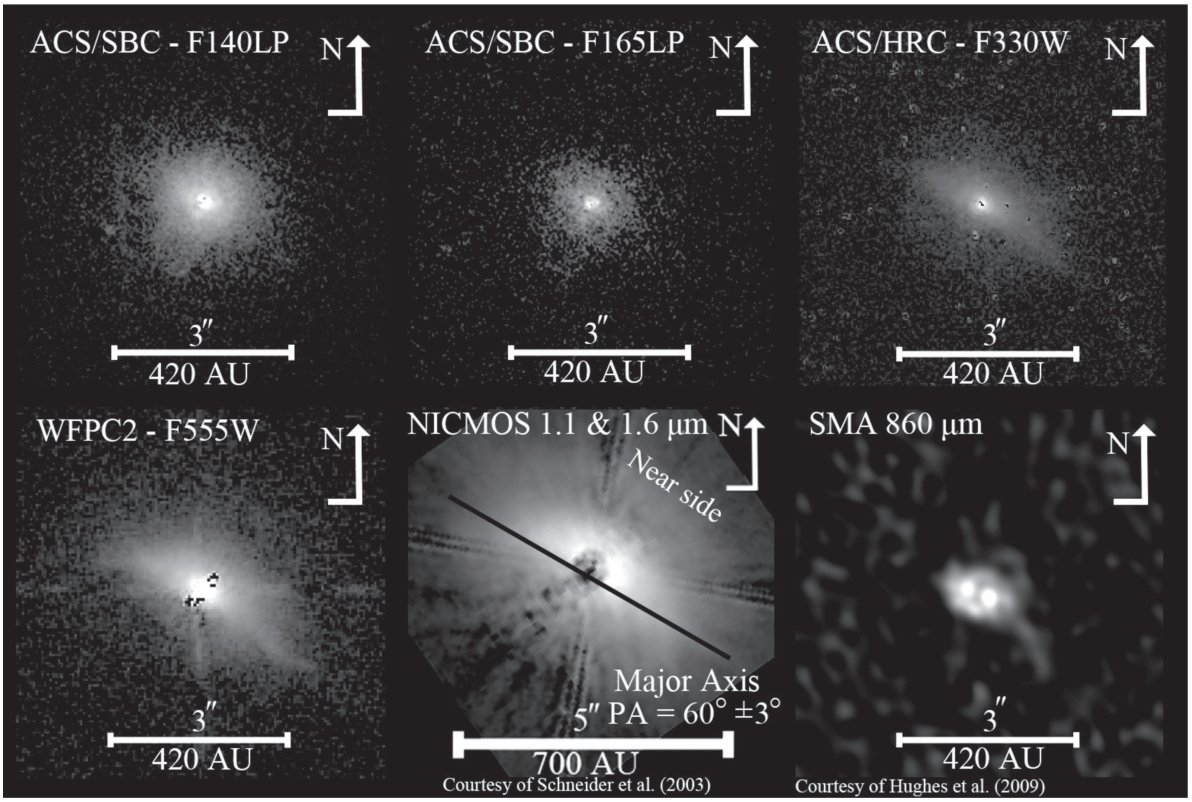

Figure 4. Top row: PSF-subtracted *HST* imagery observed in the UV with the F140LP (left), F165LP (center), and F330W (right) filters. Bottom row: PSF-subtracted *HST* imagery observed in the optical with the F555W (left, from a single exposure pair, Figure 1), the F110W and F160W combined image from Schneider et al. (2003; center), and 860 μm from the Submillimeter Array (right; Hughes et al. 2009). All panels show a $6'' \times 6''$ field of view and are oriented with north up and east to the left. Hughes et al. (2009) noted an inner cavity of size ~20 au in the 860 μm data.

Table 3
Scattered-light Properties

λ	IWA (au)	Extent[a]	Aspect Ratio	Inclination[b]	Aperture Radius	$F_{\rm disk}/F_{\rm star}$
F140LP	0.″11 (15)	…	…	…	3.″4	0.321 ± 0.12
F165LP	0.″11 (15)	…	…	…	3.″4	0.310 ± 0.08
F330W	0.″10 (14)	3.″13 ± 0.″13	0.54	57° ± 9°	3.″4	0.130 ± 0.03
F555W	0.″15 (28)	4.″16 ± 0.″10	0.59	53° ± 3°	3.″4	0.129 ± 0.03

Notes. The disk of GM Aur in the F140LP and F165LP data has features that do not allow the measurement of the extent and aspect ratio of the disk (Figure 4). The disk-scattering fraction, $F_{\rm disk}/F_{\rm star}$, is the ratio comparing the light detected from the disk between 0.″30 and 3.″4, after PSF subtraction of the light coming from the star + disk system prior to PSF subtraction. We choose the region exterior to 0.″30, rather than the IWA of each data set, so that we can compare our disk-scattering fraction results to the NICMOS results presented in Schneider et al. (2003).
[a] Full extent of the disk measured along the disk major axis; 60° ± 3° east of north.
[b] Inclination calculated from extent and aspect ratio.

detection of the disk of GM Aur over more than a decade in wavelength in comparison with the NICMOS data.

3.1.1. WFPC2/F555W

By examination of the F555W PSF-subtracted image, we estimate an effective IWA of 0.″15–0.″20 (21–28 au at $d = 140$ pc). This is about 1.5–2× the 80% encircled energy radius for the center of the PC chip (McMaster et al. 2008). To determine the radial surface brightness of the disk in the F555W data, we measured the major-axis alignment, PA = 58.°8 ± 3°, and then rotated the FITS file image to align the major axis horizontally in the frame with the location of the star in the frame center. We then calculated the median flux value (in counts per pixel) along a 3 pixel integration wide strip (0.″137 or 19 au at 140 pc) as a function of radius from the flux centroid. Using the calculated median σ value and dividing by $\sqrt{3}$ (for the integration strip width), we estimated the random error. We list results separately for the east and west sides of the disk. The resulting counts/pixel (surface brightness) versus radius relation from 0.″15 to 0.″70 was fitted to a line in log–log space with the IDL *linfit* routine, to determine the power-law index γ for surface brightness $\Sigma \propto r^{-\gamma}$. We limited the range of our line fit to radii of 0.″15–0.″70, because the fit was affected by a diffuse region of increased flux at $r \approx 0.''7$ that we cannot securely discount as an artifact. As an additional test of the major-axis alignment, we varied the FITS file rotation angle from the PA by ±5° to constrain the variation incurred along varying trial major-axis integration strips. The west side has a power-law index of $\gamma = 2.06 \pm 0.05$, whereas the east side has $\gamma = 1.63 \pm 0.06$.

Table 4
Power-law Indices for *HST* Optical Images

Filter	Rotation Offset	East Side			West Side		
		γ	Reduced χ^2	Prob	γ	Reduced χ^2	Prob
F330W	−5°	1.54 ± 0.02	2.89	0.00	2.01 ± 0.01	4.37	0.00
F330W	0°	1.41 ± 0.03	0.89	0.65	2.17 ± 0.04	1.02	0.43
F330W	+5°	1.43 ± 0.02	1.99	0.00	1.97 ± 0.02	1.90	0.00
F555W	−5°	1.67 ± 0.06	2.25	0.01	2.02 ± 0.06	0.19	0.99
F555W	0°	1.63 ± 0.06	1.54	0.12	2.06 ± 0.05	0.29	0.98
F555W	+5°	1.69 ± 0.06	0.69	0.73	2.15 ± 0.06	0.13	0.99

These results are listed in Table 4 and indicate that variations in slope arising from small changes in rotation angle are commensurate with the random (pixel) errors, at about 0.05–0.1 dex. In Figure 5 we plot the radial surface brightness profile, and we do not detect a break in the surface brightness that would indicate the presence of a cavity wall exterior to 21 au. The IWA in the F555W bandpass is not sufficiently small to eliminate the possibility of a detectable cavity for the region of the disk interior to 21 au.

3.1.2. HRC/F330W

The HRC F330W imagery is less heavily exposed than the WFPC2 data, and we estimate that it provides an IWA of 0.″1 (14 au). This corresponds to ∼40%–70% of the 80% encircled energy radius depending on whether the F330W mode behaves more like the F220W or F435W modes, which are bracketing modes plotted in Maybhate & Armstrong (2010). Similar to our F555W analysis, we determined the major axis of the disk to be aligned along PA = 59.°5 ± 3° in the F330W data. After rotating the PSF-subtracted FITS file image to align the major axis horizontally, we calculated the median flux value (in counts per pixel) along a five pixel integration wide strip (0.″125 or 17 au at 140 pc) as a function of radius from the flux centroid. Using the calculated median σ value and dividing by $\sqrt{5}$ (the integration strip width), we estimated the random error. Again for comparison, we repeated the calculation with the FITS file rotation angle changed from the PA by ±5°. The radial surface brightness (in counts/pixel) profile index along the west and east sides is $\gamma = 2.17 \pm 0.04$ and $\gamma = 1.41 \pm 0.03$, respectively. This is consistent with the east versus west difference in power-law index measured in the F555W image. Although we optimally nulled the diffraction spikes, the empirically measured σ values are small even compared to any potential Airy ring residuals (for example, at 0.″4 radius). This yields an uncertainty in the power-law fit γ value that does not include other sources of error, namely, uncertainty in PSF subtraction scaling values. While this does not alter any of our results significantly, the uncertainty in the γ values is likely larger than the formal least-squares fit error calculated by the *linfit* IDL routine.

We note no indication of a break in the radial surface brightness profile, and a smooth power-law fit lies within ∼2σ (measured empirically from pixel statistics) of the data points inward to 0.″1 (≈14 au; Figure 6). This indicates that nebulosity is present within the submillimeter cavity of GM Aur's disk. The presence of nebulosity within the submillimeter cavity/gap has previously been reported for both disks around Herbig stars (Muto et al. 2012; Grady et al. 2013) and T Tauri stars (Follette et al. 2012) in the NIR.

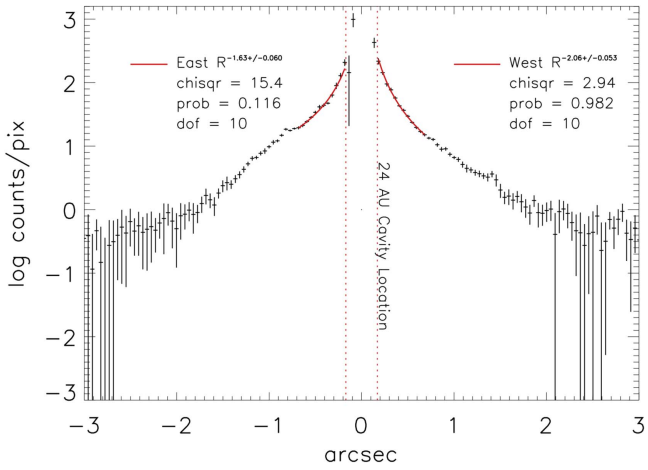

Figure 5. Radial surface brightness profile (in log counts pixel^{-1}) as measured from northeast (left side) to southwest (right side) in the WFPC2 F555W data along the disk major-axis PA = 58.°8 ± 3°. The resulting counts/pixel (surface brightness) vs. radius relation from 0.″15 to 0.″70 was fitted to a line in log–log space with the IDL *linfit* routine, to determine the power-law index γ for surface brightness $\Sigma \propto r^{-\gamma}$ (Table 4). The submillimeter cavity wall falls just within the IWA for the F555W profile. There is only one PSF star available, so we cannot show any uncertainty due to PSF template variations.

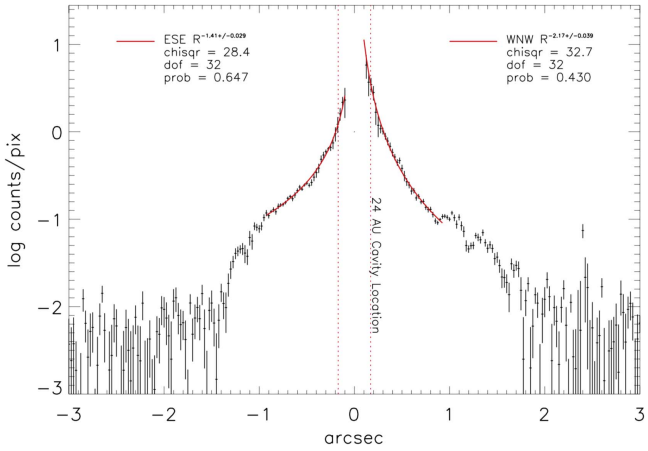

Figure 6. Radial flux profile (in log counts pixel^{-1}) along the disk (northeast to left, southwest to right) major axis (PA = 59.°5 ± 3°) as measured in the ACS/HRC F330W data. The best fits to these data are calculated from the IWA 0.″10 to 1″ using the IDL *linfit* routine. The 24 au cavity seen in the submillimeter (Hughes et al. 2009) is not detected in the radial brightness profile of the F330W data. The main point of this figure is to show the *lack* of a break in the radial surface brightness profile *inside* of the purported cavity. This lack of a break is unlikely to be a consequence of a poor choice of PSF template.

This is the first report of a similar phenomenon in the optical and FUV.

3.2. Geometrical Constraints on the Disk in Scattered Light

Disk geometry can be determined by power-law fits to its radial surface brightness (SB) profile (Grady et al. 2007; Wisniewski et al. 2008). Geometrically flat or minimally flared disks with an outer wall structure, where the walls do not shadow the outer disks, result in power-law fits of $\approx r^{-3}$ to their radial SB profile (e.g., HD 100546, Grady et al. 2001; HD 169142, Grady et al. 2007; HD 97048, Doering et al. 2007; HD 163296, Wisniewski et al. 2008). In contrast, the disk of GM Aur has the morphology of a flared disk seen in scattered light, i.e., brighter along the forward scattering (north side) semiminor axis, and bilaterally symmetric about the minor axis in surface brightness distribution (Whitney & Hartmann 1992; Stark et al. 2006). The power-law fit to its radial surface brightness profile of $\approx r^{-2}$ is further evidence that the disk of GM Aur is flared.

The surface brightness profile of the disk from the ACS/HRC F330W data also lacks any evidence of the 24 au cavity that was observed by Hughes et al. (2009) at submillimeter/millimeter wavelengths. The nondetection of a change in the power-law fit to the surface brightness profile at or near 24 au and the fact that *we do not see diffraction spikes* indicate that the disk is optically thick inside this radius at these wavelengths. We conclude that in the FUV we see scattering from particles on the order of the observed wavelengths (Whitney & Hartmann 1992), where the morphology displays the characteristic pattern of a flared disk. We therefore infer that we observe light scattered by submicron-sized grains within the 24 au submillimeter cavity. This conclusion was also reached by Calvet et al. (2005).

3.3. Grain Properties

Monochromatic imaging is insufficient for characterizing a particle size distribution because the relationship between the grain opacity/albedo and particle size is degenerate (Watson & Stapelfeldt 2007). However, multiwavelength imaging can break this degeneracy if done over a sufficiently wide wavelength range. Our data extend the wavelength coverage for GM Aur by an order of magnitude. Schneider et al. (2003) modeled the disk of GM Aur exterior to 0.″3 (thus exterior to a 24 au disk) and were able to accurately reproduce the size, overall brightness level, large-scale surface brightness distribution, etc. using a grain model with a maximum radius of 1 mm, an exponential cutoff scale length of 50 μm (Model 1 in Wood et al. 2002b), and a minimum grain size of 0.05 μm (M. J. Wolff & K. Wood 2016, private communication). Schneider et al. (2003) measured the disk-scattering fraction, the ratio of light scattered by the disk to starlight ($F_{\rm disk}/F_{\rm star}$). We also measure $F_{\rm disk}/F_{\rm star}$, (1) because it is an extinction-free parameter, (2) because it is a measurement of the disk albedo, (3) to determine how $F_{\rm disk}/F_{\rm star}$ varies as a function of wavelength, and (4) to compare the result with grain opacity models and constrain possible grain compositions. We note that $F_{\rm disk}/F_{\rm star}$ applies to the disk surface, at distances of ~50–1000 au, so any short-term (<0.5 day) variability from flares should not affect it significantly.

If the dust grain model from Wood et al. (2002a) used in Schneider et al. (2003) is correct, the disk dust opacity would exhibit a shallower wavelength-dependent opacity than the canonical interstellar medium extinction curve (Cardelli et al. 1989). To examine the wavelength dependence of the resultant scattered light, we determined $F_{\rm disk}/F_{\rm star}$ for the F140LP, F165LP, F330W, and F555W images as follows. For the disk flux, we measured aperture photometry from 0.″3 out to a radius of 3.″4, with a sky annulus of 4″–6″, in the PSF-subtracted image. Results were not sensitive to the choice of the sky annulus. For the stellar flux comparison, we measured the flux in the entire region out to 3.″4 in both the scaled PSF template data and the GM Aur data without PSF subtraction. The stellar flux strongly dominates over the disk flux. We then determined $F_{\rm disk}/F_{\rm star}$ uncertainties for the F330W and F555W bands, where there are diffraction spikes, based on the PSF subtraction scale factor uncertainty (the dominant uncertainty in the flux). This was set by requiring that the residual diffraction spikes be within 1σ (rms) of the local mean (Section 2.2). For the F140LP and F165LP bands (discussed in detail in Sections 3.4 and 4.3), we constrained the uncertainty in $F_{\rm disk}/F_{\rm star}$ using the lower and upper bounds of the scale factor used for the PSF template. There are no diffraction spikes in these data (see Section 2.3 for details). We supplement our values with measurements for the F110W and F160W bands from Schneider et al. (2003) of 0.025 ± 0.005 (20%).[26] Values for $F_{\rm disk}/F_{\rm star}$ are listed in Table 3 and plotted in Figure 7. This figure also shows dust grain opacity curves that represent a range of grain size distributions and compositions.

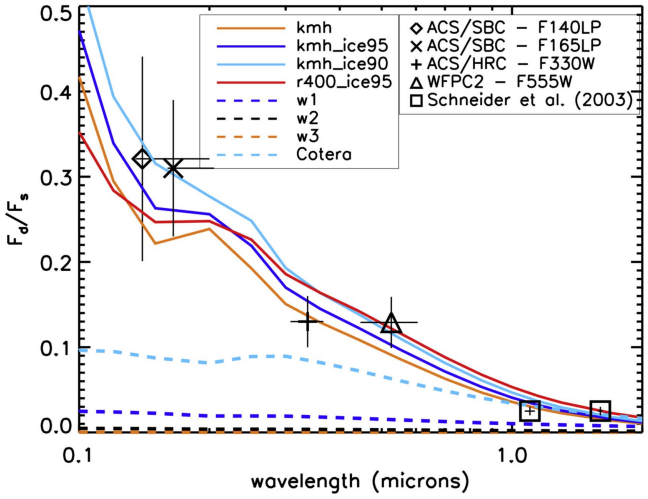

Figure 7. Disk-scattering fraction at the disk surface $F_{\rm disk}/F_{\rm star}$ as a function of wavelength has been measured and compared with grain opacity models that have varying grain size distributions. The w1, w2, w3, and Cotera models are models 1, 2, 3, and Cotera from Wood et al. (2002b), respectively, and they have size distributions dominated by large (micron-sized) grains or larger and result in gray scattering (flat curve). The r400_ice95 model is a standard one offered in the 2014 version of HOCHUNK3D (Whitney et al. 2013), adopted from Whittet et al. (2001) and modeling total-to-selective extinction of $R_V = 4$, corresponding to dense regions of star-forming clouds with optical depth $\tau_{3.0}$ for the 3 μm ice absorption feature. The r400 model and the kmh models have size distributions similar to that of the ISM, with variations in composition, and their scattering efficiency increases rapidly at shorter wavelengths. See Section 3.3 for additional details.

The grain opacity profiles in Figure 7 have been scaled to fit our measurements and those of Schneider et al. (2003). The

[26] Schneider et al. (2003) also give a value of ≈4%. After private communication, we learned that this is an error and should have read ≈2.5%.

grain opacity models kmh, kmh_ice95, and kmh_ice90 originate from Kim et al. (1994) and are representative of ISM-like grains. The _ice## extension indicates a water ice coating on the grain surface. The number indicates the ratio of grain material to water ice, where ice90 is 90% grain and 10% water ice coating on the grain surface, ice95 is 5% water ice, etc. Models 1, 2, 3, and Cotera in Wood et al. (2002b) correspond to w1, w2, w3, and Cotera, respectively, in this paper and are grain models dominated by large dust grains. These large grain models are described in detail in Wood et al. (2002b) and Cotera et al. (2001). All models in Wood et al. (2002b) are composed of amorphous carbon–silicon, and they are dominated by micron-sized grains or larger (min = 0.05 μm, max = 1 mm). We rule out the w1, w2, w3, and Cotera models as candidates for the surface grain composition of GM Aur, at approximately the 4σ level for the Cotera grain model, and at the 7σ level for the others, based on our scattered-light measurements of the disk in the F140LP, F165LP, F330W, and F555W data (Figure 7). To compare the disk-scattering fraction with the grain opacity of the models, we scaled the grain models to fit the data points given in Schneider et al. (2003) and the F330W and F555W data, because the FUV data have larger errors. The kmh models and the r400 model all lie close to the values for $F_{\rm disk}/F_{\rm star}$ we have measured, but the uncertainty in our values is large enough that we cannot decide conclusively between these models. However, the only grain model with an opacity curve that fell inside the error bars of all of our $F_{\rm disk}/F_{\rm star}$ measurements was the kmh_ice95 model. The wavelength dependence of the disk-scattering fraction we find indicates that the disk surface is populated with grains that have a size distribution similar to that of the ISM, both in the outer disk and within the region of the submillimeter cavity. It is possible that the physical grain population at the surface of the disk differs in composition from the grain models we have presented. However, if so, we can exclude pure frosts of H_2O, CO_2, NH_3, and SO_2. The reflectance measured for each of these pure ices is flat in the optical and slightly rising to its peak at $\approx$0.2 μm (except SO_2, which remains flat) before each drops rapidly to its minimum reflectance at $\approx$0.16 μm (Hapke et al. 1981). These same disk models were then used to construct a synthetic image, discussed in Section 4.3.

3.4. Structure Unique to the FUV

Initial inspection of the PSF-subtracted ACS/SBC data unexpectedly revealed an extended structure that is not detected in any of the other bandpasses. The disk seen at these shorter wavelengths appears cylindrical in shape and limb brightened (Figure 4; top left and top middle panels). The structure is detected strongly in the F140LP bandpass, containing ~10% of the flux in the star+disk. It is also seen marginally in the F165LP bandpass and can be traced out $1\farcs1 \pm 0\farcs2$ along PA $150^\circ \pm 5^\circ$ away from the disk midplane (along the southeastern semiminor axis). Deprojecting our measurements to determine a physical size of the structure, we find that it extends to a height 190 ± 35 au above the disk midplane. The wall thickness of the feature, or equivalently the area where we detect limb brightening, is $0\farcs17 \pm 0\farcs05$ or 24 ± 7 au. The radial brightness of the feature, measured along the area where it is limb brightened, decreases as $r^{-0.7\pm0.1}$. We measure the outer radius of the feature to be $0\farcs46 \pm 0\farcs05$ (64 ± 7 au). From this we calculate that the inner radius is 40 ± 10 au, which corresponds to the inner region of the outer disk just beyond the radius of the submillimeter cavity wall. The abrupt appearance of this structure in the ACS/SBC data is consistent with the source being seen in emission.

As a transitional disk, GM Aur is beyond the evolutionary stage where an outflow cavity with a narrow opening angle would be expected (Seale & Looney 2008), and the cylindrical geometry of the structure is inconsistent with the parabolic or "V"-shaped geometry that is characteristic of outflow cavities in younger systems. This shape is also inconsistent with the typical appearance of an atomic or ionic jet, i.e., a collimated signal aligned along the minor axis. The main optical jet diagnostics are high-velocity emission in the lines of [O I] λ6300, [N II] λ6580, [S II] $\lambda\lambda$6731, 6716, and Hα. In GM Aur, there is no evidence for a high-velocity component (indicative of a collimated jet) in these lines (Hartigan et al. 1995). We see no such collimated signal (also see Cox et al. 2007).

Another argument against an ionic jet would be that the forbidden emission line [O III], which sometimes may be found in jets (albeit requiring high-velocity shocks of $v > 100$ km s^{-1}), would be detected in the F555W bandpass (McMaster et al. 2008) as a collimated source aligned along the system minor axis. Again, no such collimated signal is detected in the WFPC2 data, and the structure detected in the SBC data does not exhibit the typical jet morphology. The fact that the structure is not detected in a bandpass dominated by reflection nebulosity indicates that the source is not predominantly dust. It is unlikely that very small grains (transiently heated) could produce the diffuse UV emission, because the flux from the star is insufficient. In addition, the small-grain thermal emission would have the morphology of the disk—which is not the case for UV emission around GM Aur. The source of the emission can be investigated more thoroughly with long-slit spectroscopy; we discuss the possibility that the emission may arise from H_2 in Section 4.3.

3.5. SED and Model Image

We modeled the SED and images of GM Aurigae using the 2013 version of the Whitney Monte Carlo radiative transfer (MCRT) code (Whitney et al. 2013). The SED was fitted to the data mentioned in Section 2.4 (Figure 8). Fitting a model SED to an observed SED is not conclusive on its own due to the degenerate nature of the SED inherent from the vast parameter space (Chiang et al. 2001; Robitaille et al. 2007). Comparison of model data to the corresponding observational imagery and our $F_{\rm disk}/F_{\rm star}$ measurements can reduce the number of free parameters. The stellar parameters were largely determined by the value of $A_V = 0.1$ we chose based on the extinction stated in France et al. (2014); a larger value would have been less consistent with the FUV flux. Hughes et al. (2009) give $T = 4730$ K, $R = 1.5\ R_\odot$, $d = 140$ pc, and $A_V = 1.2$, Hueso & Guillot (2005) use $T = 4060$ K, $R = 1.83\ R_\odot$, and $d = 140$ pc, and Pott et al. (2010) employ $T = 4730$ K, $R = 1.5\ R_\odot$, and $A_V = 1.2$. Our best-fit model to the SED shape indicated parameters of $T = 4000$ K, $M = 1.2\ M_\odot$, $R = 1.5\ R_\odot$, and $A_V = 0.1$. The presence of FUV flux supports the lower value of A_V we choose, which requires a cooler star to give the correct stellar contribution to the SED. We employ a disk cavity size out to 24 au (Calvet et al. 2005; Hughes et al. 2009; Andrews et al. 2011; Gräfe et al. 2011). The only free parameter left for the star is the distance, which scales the model spectrum. This constrains $d = 148$ pc for our models,

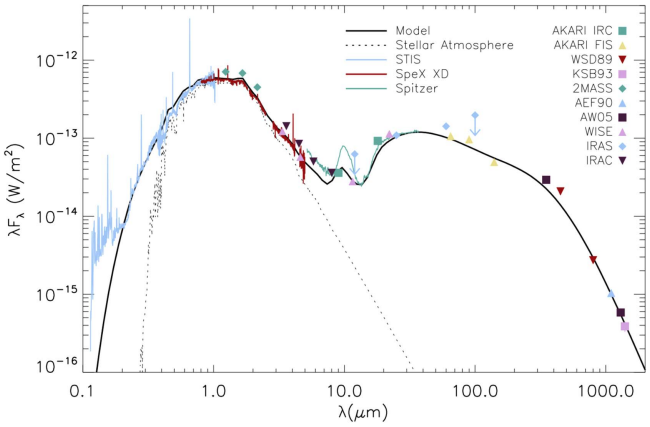

Figure 8. SED of GM Aur using data discussed in Section 2.4 and best-fit MCRT model (solid black line; see Section 3.5). The X-ray flux is 6.82×10^{-16} W m^{-2} at $\lambda \approx 0.0021$ μm (Güdel et al. 2010) and would be consistent with an extrapolation of the UV flux; we do not plot it as it would crowd the other data points into one quadrant of the panel. Paper references are WSD89—Weintraub et al. (1989); KSB93—Koerner et al. (1993); AEF90—Adams et al. (1990); AW05—Andrews & Williams (2005). The SPEX and STIS data are from 2011.

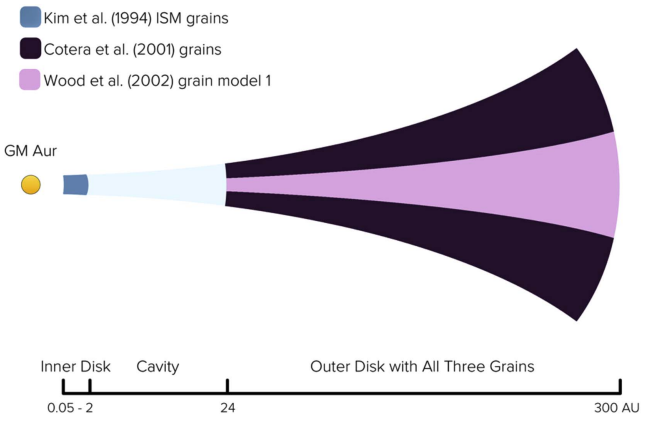

Figure 9. MCRT code from Whitney et al. (2013) was used to model the disk of GM Aur, and this schematic illustrates the basic parameters involved. There is an inner disk that extends from 0.5 to 2 au, and then a gap devoid of material extends out to 24 au, followed by a flared outer disk with two dust components. The disk midplane is dominated by large grains used to model the edge-on disk of HH30 (Model 1; Wood et al. 2002b). Above the midplane, the outer disk has two components. The grains described by Cotera et al. (2001) have a size distribution smaller than the grains at the midplane, but larger than ISM-like grains. This region also contains a population of ISM-like grains *(not shown via shading)* and is described by Kim et al. (1994).

which is within the uncertainty of the distance (Bertout & Genova 2006). We find evidence for variability in the NIR and UV portions of the SED (Figure 8). The high accretion state corresponds to the 2MASS data and *Spitzer*-era observations (IRAC from 2004, IRS from 2005). The variability is described in detail in Ingleby et al. (2015).

The disk itself was modeled to match the observed SED with three components (Figure 9). The first is an inner disk composed of the grains of Kim et al. (1994), primarily fixed by the 10 μm strong silicate feature we see in the data, which extends from the sublimation radius out to 2 au. This inner disk is composed of kmh grains (Kim et al. 1994) and contributes 4×10^{-7} of the overall disk mass, which is 0.092 $M_{\odot}$ *in total*. The $r = 2$ au radius for the inner disk is motivated by the model used by Calvet et al. (2005), whose inner disk region was less than 5 au. This size is consistent with the 10 μm emission (Hughes et al. 2009) and is otherwise optically thin in the IR, as was the model disk for Calvet et al. (2005). It is not necessarily optically thin in the UV and at blue optical wavelengths. In that case, in the more optically thick UV we see the outer layers of the disk, while at longer, more optically thin wavelengths we see deeper into the disk (Pinte et al. 2008; e.g., see their Figure 6 caption).

The second component was a disk settled near the midplane composed of the grain prescription of Wood et al. (2002b), to match the SED at millimeter wavelengths. The disk contained 0.07 $M_{\odot}$ (i.e., ~80%) of the total disk mass and extended from 24 au to an outer disk radius of 300 au. This grain type and mass fraction were chosen in order to fit the millimeter-wavelength data effectively. Lastly, a second outer disk extending vertically off the midplane was composed of the grains of Cotera et al. (2001), also extending from 24 to 300 au. The Cotera grains were adopted because they best fit the SED complementary to the millimeter region produced by the outer disk regions. We know that something kmh-like must exist in the inner disk region given the very strong silicate feature, and for simplicity's sake, a disk composed of kmh grains throughout was attempted. However, this just did not produce a good fit within the other constraints of the model. In the end, a larger grain-settled disk composed of Wood et al. model 1 grains with a Cotera jacket and some kmh grains throughout produced the best fit. Other grain composition/distribution models may also work. The icy kmh grains are the best fit to the observed $F_{\rm disk}/F_{\rm star}$. The amount of allowed parameter space for grain types and distribution characteristics may be large, and we defer more detailed modeling to a subsequent paper.

Two hot spots were also added on the star: one facing toward and another away from the observer. The hot spots along with an accretion rate of $\dot{M} = 4 \times 10^{-9}$ $M_{\odot}$ yr^{-1} served as a source of FUV emission needed to fit the STIS data set portion of the SED. The code was run with 2×10^9 photons for the image models, which was the maximum permissible in the version of the code available.

The Whitney code comes with predefined filters that mimic the throughput of filters commonly used in observations. Our novel approach is the first to require FUV filters, which are not included with the code. The code does, however, allow the creation and implementation of user-defined filters. We thus added filters using the throughput curves for the F140LP and F165LP filters in the ACS Instrument Handbook (Maybhate & Armstrong 2010). We convolved the model images with a Gaussian filter (GFILTER), from the IDL IUELIB astronomical library.[27] The FHWM of the PSF star images for F140LP, F165LP, and F330W were measured with the IRAF IMEXAM routine,[28] yielding Gaussian approximations of 0.″10, 0.″09, and 0.″06, respectively. We used half those values as the standard deviation for the GFILTER input, using enough points to go out ~4 standard deviations when filtering the model images. We then used the ARTDATA routine to add noise to the F330W model and background pixels from the SBC data for

[27] www.astro.washington.edu/docs/idl/cgi-bin/getpro/library38.html?GFILTER

[28] IRAF is distributed by the National Optical Astronomy Observatories, which are operated by the Association of Universities for Research in Astronomy, Inc., under cooperative agreement with the National Science Foundation.

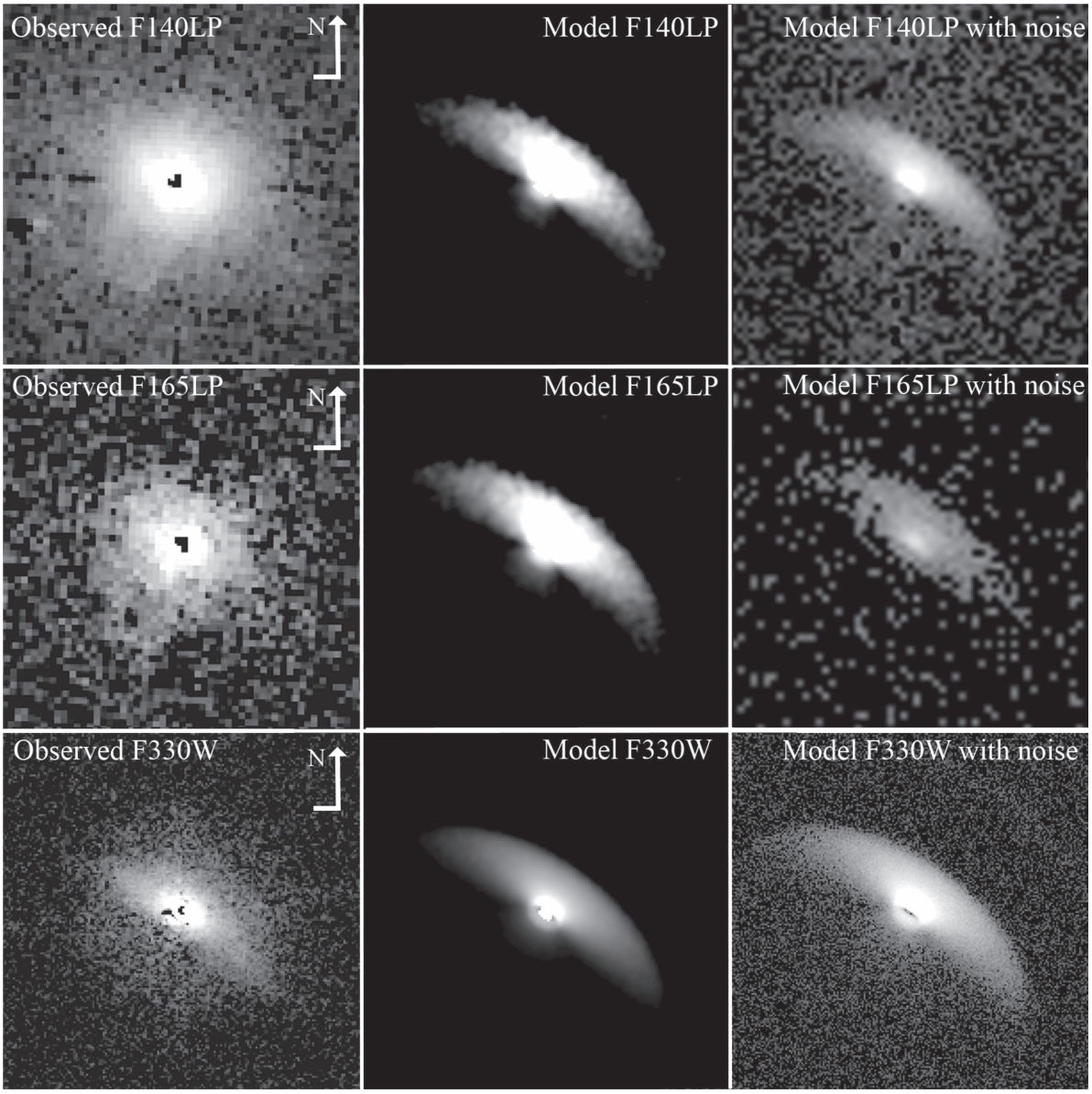

Figure 10. Comparison of PSF-subtracted ACS images for GM Aur (left panels) and Whitney code models rotated and scaled to match the images (right panels) for F140LP, F165LP, and F330W (top to bottom). Field sizes are 600 au for the models and 4.″0 for the images (600 au at 148 pc). North is up and east to the left in all panels. The models and the images generated from them are consistent with the GM Aur SED (see text for details), with the possible exception of accounting for all of the UV excess (involving F140LP and F165LP). The emission to the SE of the disk in those two filters is apparent in the data, but not in the models.

the F140LP and F165LP model images. Finally, we subtracted the appropriate PSF templates from the images.

For the F330W model, the image appears to match the data reasonably well outside of a radius of $r \sim 0.''2$ (Figure 10). Interior to that point, the gap and inner rim of the disk are visible in the F330W model image, whereas we find no indication for any gap or rim in the actual image data, nor from the radial surface brightness profile from the data (Section 3.1.2; Figure 11). The F165LP model image bears less resemblance to the image data than for the F330W case, and the data appear much more circular than the model due to emission to the SE. For the F140LP model image, the difference is even more pronounced, with the cylindrical projection form to the SE showing more clearly in the observed data, plus perhaps a smaller amount of diffuse emission to the NW. Although the disk morphology is well fitted at wavelengths $\lambda > 3300$ Å, we cannot model the observed FUV emission well using only scattered light. There is an extra emission component along the minor axis that could be consistent with an outflow, which is not included in the model.

4. DISCUSSION

The disk of GM Aur has now been detected in scattered light from 0.1450 to 1.6 μm, more than a decade in wavelength coverage. This large-wavelength lever allows us to explore the surface dust grain opacity as a function of wavelength, in a manner similar to Pinte et al. (2008) but with the addition of FUV wavelength coverage. In contrast to Schneider et al. (2003), who inferred a dust grain composition similar to model 1 in Wood et al. (2002b), which is composed of large grains (up to 1 mm), we find that the wavelength dependence of $F_{\rm disk}/F_{\rm star}$ is consistent with ISM-like grains. This indicates that little grain growth has occurred in the upper layers of the disk. ISM-

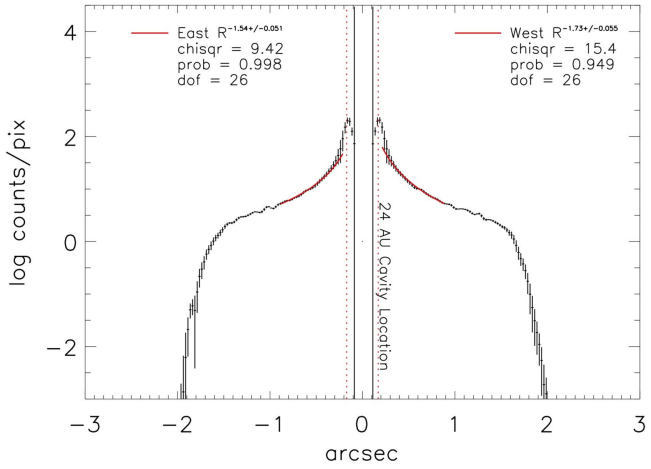

Figure 11. Same radial brightness profile calculation as in Figure 6 on the model F330W image. The 24 au cavity seen in the submillimeter (Hughes et al. 2009), which was not detected in the F330W data, is detected in our model image data. Consequently, the best fit to the model image required a starting point exterior to the cavity location; the fit from $0\farcs2$ to $0\farcs9$ is shown here.

like grains are also consistent with the radial surface brightness profile of the disk at 3300 Å. The overall color of the dust disk surface is blue ($m_{\rm F330W} - m_{\rm F555W} \approx -0.2$), and the presence of ISM-like grains is undoubtedly a factor in disk detection in direct imaging using WFPC2 (Stapelfeldt et al. 1995).

4.1. Cavity Nondetection at Short Wavelengths

The cavity detected in millimeter, submillimeter, and mid-IR wavelengths (Calvet et al. 2005; Hughes et al. 2009; Andrews et al. 2011; Gräfe et al. 2011) is large enough in radius to be detected in the FUV and optical F330W bandpasses. The consistency in detections of the cavity at mid-IR and longer wavelengths makes it safe to assume that there is a cavity in the large grain dust. However, we report a nondetection of the cavity exterior to 15 au at optical and FUV wavelengths. Our analysis provides no evidence for a break in the radial surface brightness profile that would indicate a depletion in the surface density of the grains or signal the presence of a change in disk composition. This can only be the case if the small grains at the surface of the disk persist inside the radius of the submillimeter cavity wall. Our nondetection of the cavity indicates that there is a mechanism in place actively filtering the material within the cavity, allowing only submicron grains to migrate inward beyond the cavity wall. (This is not precluded by the SED fit and does not conflict with a statement by Calvet et al. [2005] on the outer boundary of the optically thin region in the IR and/or redward. The inner region is optically thick in the FUV.) This conclusion is supported by the analysis of rovibrational CO lines in Salyk et al. (2011). Their models suggest that an inner disk of CO gas extends out to a radius of 0.2 au of GM Aur, and that it is likely being replenished via gas migration through the cavity from the outer disk. This is consistent with MCRT and hydrodynamical model predictions in Paardekooper & Mellema (2006), Rice et al. (2006), Zhu et al. (2012), Dong et al. (2012), and de Juan Ovelar et al. (2013), which suggest giant planet formation within the disk cavity as a likely culprit in this scenario. There are other mechanisms that can also preferentially decrease the density of micron-sized grains. Grain growth is one possibility, although it could be expected to vary smoothly with radius (Cieza et al. 2012). Dullemond & Dominik (2005) concluded that if grain growth were responsible for cavity development, small grains must be replenished, possibly by aggregate fragmentation via high-speed collisions. Owen et al. (2011) suggested that X-ray photoevaporation could explain a large fraction ($\gtrsim$50%) of transitional disks. However, Alexander et al. (2006) suggested that GM Aur in particular had too high an accretion rate to have its cavity produced by photoevaporation, and that it was rather caused by another mechanism such as planet formation or grain growth/coagulation. The detection of small dust grains within the millimetric cavity seems to rule out photoevaporation and dust coagulation processes as the main origin for the millimeter feature, as in both cases small dust particles would not be expected inside the hole. Our result here confirms the predictions of Calvet et al. (2005) and Espaillat et al. (2010), using an independent data set.

4.2. Limits on Giant Planets in the Disk of GM Aur

Grain filtration occurs when larger grains are restricted to the outer disk and small grains, which are more tightly coupled to the gas, can freely penetrate the cavity (Rice et al. 2006). Grain filtration is also a predicted consequence of the presence of one or more giant planets. Based on the models presented in Zhu et al. (2012), a 3 M_J object would clear a gap in the 30 μm grains on a timescale of 10^5 yr and create a noticeable depletion ($\approx$3 orders of magnitude) in the gas density within the cavity. The models presented in de Juan Ovelar et al. (2013) produce similar results to those given in Zhu et al. (2012). They find that a 1 M_J planet does deplete 1 μm sized grains at the surface of the disk that could be detected in optical (0.65 μm) observations (de Juan Ovelar et al. 2013, Figure 3), given high enough spatial resolution. They find that a 9 M_J planet depletes the 1 μm grains at the disk surface by a factor of 1000 (de Juan Ovelar et al. 2013, Figure 7) at the planet location; a 15 M_J planet eliminates dust grains of all sizes entirely from the disk surface at the location of the planet. Their results suggest that a planet with a mass $>9\,M_J$ at $\approx$20 au would create a depletion in submicron surface grains that would be detectable in our PSF-subtracted 1400, 1650, and 3300 Å data. However, a depletion is not detected in our UV or optical observations, and its absence places an upper limit on the mass of a planet in the disk of GM Aur to a mass of $<9\,M_J$, likely even lower, though the model grid is too course to be more specific. Furthermore, the models by Zhu et al. (2012) and de Juan Ovelar et al. (2013) also place a 1 M_J lower limit on planet mass due to the detection of a cavity in millimeter and submillimeter data (Calvet et al. 2005; Hughes et al. 2009; Andrews et al. 2011; Gräfe et al. 2011).

4.3. A Possible Molecular Outflow

Molecular outflows launched from the inner disk are expected in very young star + disk systems (Ercolano et al. 2009), but their persistence in older systems is less well explored. Extended H_2 emission has been detected around a host of young objects, for example, RU Lupi (different signals in different apertures; Herczeg et al. 2005), plus T Tauri (Saucedo et al. 2003; Walter et al. 2003) and DG Tau (Schneider et al. 2013). Spectroscopically, it is clear that the H_2 is coming from an emitting region that is not from the star but rather from the inner part of the disk; thus, it is extended

spatially. For DG Tau, the UV H_2 emission appears as a limb-brightened "bubble" with a length of about $0\farcs3 = 42$ au located toward the approaching lobe of the outflow. A very similar morphology is observed in the NIR (Agra-Amboage et al. 2014). The H_2 emission lines in several systems are also red/blueshifted, which is expected in the case of molecular outflows (Herczeg 2005; Herczeg et al. 2006; France et al. 2012); Herczeg et al. (2006) discuss the spectral evidence for other potential sources of H_2 emission as well. France et al. (2012) found no clear evidence for extended UV fluorescent H_2 emission lines for GM Aur in their Cosmic Origins Spectrograph (COS) data around 1450 Å. The COS line profiles they present do not show obvious extended wings, though there may be a hint of marginal additional flux at -30 to -40 km s^{-1} in their Figure 3. Otherwise, they are centered at the systemic velocity and appear compatible with emission from the inner disk (at radius 0.5 au). Their analysis was designed to map the distribution of H_2 in the disk, assuming Keplerian motion of the fluorescent gas.

As discussed in Section 3.4, we detect an extended signal aligned along the disk's semiminor axis in the F140LP and F165LP data that we do not detect in any other bandpass. This structure projects beyond the boundary where we expect to observe reflection and scattered light from the disk surface. The protruding region of the feature is limb brightened, and its geometry appears cylindrical with a radius of 40 ± 10 au. A possible interpretation is that it is a gaseous photoevaporative wind of H_2, with some of the smallest submicron dust grains embedded within, being driven from the disk surface just beyond the location of the 24 au submillimeter cavity. We only detect the feature in the observations where numerous H_2 transitions exist (in the FUV), indicating that its composition could be primarily molecular hydrogen. The smallest dust grains are the most tightly coupled to the gas, so without detection in the F330W data, any dust grains embedded within the gas must be either small in radius or low in abundance. The structure, being aligned with the system minor axis, may offer an explanation for the 5″ distant "polar lobes" seen in the NICMOS data (Schneider et al. 2003), which they interpreted as likely due to shocked line emission from a molecular outflow. We exercise some caution in this interpretation, subject to confirmation of this feature, which would benefit from more detailed modeling and further FUV spectroscopy specifically designed to cover the candidate outflow region.

The dominant excitation mechanisms in classical T Tauri stars are the high-energy X-ray and EUV photons that are produced during accretion. These high-energy photons photo-dissociate molecular gas and excite the atomic components that remain, so they are easily detected in the optical forbidden emission lines O I, S II, etc. (Schneider et al. 2013). Strong UV C IV, He II, Si IV, and N V lines have been detected toward GM Aur (Ardila et al. 2013). Furthermore, Schneider et al. (2013, their Figure 2) show the bandpass of the F140LP and F165LP filters superposed on the spectrum of the active T Tauri star DG Tau. C IV, He II, and Si IV emission may also contribute to the flux in the F140LP filter. The C IV lines are the strongest features longward of 1300 Å, but as noted in France et al. (2012), the integrated H_2 flux is twice that of the C IV doublet. However, we have not detected any extended atomic or ionic emission lines in the broadband optical WFPC2 imagery or UV/optical STIS spectra, and we conclude that it is not an atomic or ionic jet that is responsible for the extended emission detected in the FUV ACS/SBC data. For clarification, we follow the terminology convention of Klaassen et al. (2013), Ray et al. (2007, p. 231), and Reipurth & Bally (2001) and define a jet as high-velocity gas (>100 km s^{-1}) launched from the inner 0.1 au of the disk, collimated by the magnetic field. The geometry of the outflow is inconsistent with typical collimated atomic jets. The outflow appears to launch from the inner portions of the outer disk rather than the central star and smoothly extends 190 ± 35 au until it is no longer detectable above the background. There is also no detection of accompanying H I in the outflow, so it is likely that the material does not dissociate, which precludes X-ray and EUV as the excitation mechanism. H_2 is far more likely this far out from the star rather than hot (up to 10^5 K) gas. The hot transition region lines (C IV, Si IV) seem to be emitted from the stellar surface, while the molecular lines are circumstellar. These are further arguments against the possibility that the source of the emission is hot. It is possible that the H_2 is being excited by FUV photons at Lyα. If it is fluorescently excited by Lyα from the vicinity of the star, we should expect the radial brightness of the structure to decline as $\approx r^{-2}$. However, we find that the radial profile of the structure follows an $r^{-0.7\pm0.1}$ dependence. One possibility this implies is that some fraction of the fluorescent excitation could be shocked gas (Herczeg et al. 2002).

GM Aur may possibly present the first direct detection of the dominant mechanism responsible for clearing gas from the outer disk. If this phenomenon were representative of other transitional disks at 1–2 Myr, then it would place tight constraints on the time frame over which gas giants may form. How common this could be among transitional disks and over what portion of a disk's lifetime this continues are points that can only be addressed with observations of additional transitional disks in the FUV.

4.4. Summary of Results

1. We confirm previous results for disk orientation and inclination, but at shorter wavelengths than those in the literature. Additionally, we have combined multiple data sets from the literature and unpublished data to create a detailed SED that spans nearly 4 orders of magnitude (from 0.14 to 860 μm).
2. We resolve the disk down to a radius corresponding to 15 au (the distance to GM Aur assumed to be 140 pc) in optical and FUV wavelengths. We do not detect a change in the radial surface brightness profile at or near the location of the submillimeter cavity wall. We conclude that small-grain dust and gas exist within the cavity, which is consistent with models that describe dust filtration via planet–disk interaction (Dong et al. 2012; Zhu et al. 2012; de Juan Ovelar et al. 2013).
3. Comparing the surface brightness of the disk imaged at the multiple wavelengths discussed here and reported in Schneider et al. (2003) with grain models (see Whitney & Hartmann 1992; Kim et al. 1994; Cotera et al. 2001; Wood et al. 2002b), we conclude that the surface of the disk is populated by small grains.
4. The FUV observations detect a signal, undetected at longer wavelengths, that extends along the disk semi-minor axis. One possible explanation we put forth is that it is an FUV photoevaporative disk wind composed of H_2 and small-grain dust. However, radial velocity

measurements along with additional FUV long-slit spectral data are needed in the future, in order to test this hypothesis.

4.5. Implications for the Future

As mentioned in Section 4.3, small-scale H_2 molecular outflows have been detected in T Tauri stars, especially in the NIR (Beck et al. 2008, 2012), but also in the FUV (DG Tau; Schneider et al. 2013). They could be something other than thermally driven winds. For example, at $r = 40$ au around a $1.2\,M_{\odot}$ star the escape velocity would be $v_{\rm esc} \sim 7$ km s^{-1}, which would require a gas temperature $T_{\rm gas} > 5000$ K, high for the molecular gas component. GM Aur allows possibly the first direct imaging detection of such a molecular outflow from a T Tauri star in the FUV. If confirmed in future observations of GM Aur, its presence would have far-reaching implications. Observations with ALMA could determine the abundance and chemical composition of GM Aur's disk, as well as provide high-precision radial velocity data for the gas in the extended region (Klaassen et al. 2013; Mathews et al. 2013; Bruderer et al. 2014). In the past, a topic of much speculation has been over what time frame and by what mechanism gas is cleared from the outer disk. H_2 is the dominant gas species in disks. Therefore, if this outflow feature is composed primarily of H_2 and found in future observations to be present at an early age for a significant number of star + disk systems, it will constrain the time frame over which gas giants may form. ALMA data could also have an impact on how we approximate gas-to-dust ratios in MCRT and hydrodynamical models of transitional disk systems (Bruderer et al. 2014).

When available, high-contrast imagery in FUV and short-wavelength optical bandpasses enhances our ability to determine whether small-grain dust exists within the cavities of transitional disks. Transitional disks with larger cavities than GM Aur would constrain the dust opacity and particle size distribution, as well as place limits on the ice content at the dust disk surface. Higher signal-to-noise ratio data, such as might be provided by the next generation of UV instrumentation, are needed to probe ice chemistry in the outer dust disk surface. They could also more stringently constrain the contribution of pure ice grains from the most abundant ice species. Converting flux data into mass-loss rates—which can then be quantitatively compared with predicted photoevaporation and photodissociation rates—requires velocity data at the location of the molecular H_2 outflow. The loss rate of the dominant gas species in the disk is directly related to the time allowed for gas giant formation. It is important for transitional disk investigators to fully explore the feasibility of obtaining high-contrast FUV imagery on these objects while the opportunity exists, as there is no approved successor to *HST* with an FUV imaging capability.

This work is, in part, based on observations made with the NASA/ESA *Hubble Space Telescope*, obtained at the Space Telescope Science Institute, which is operated by the Association of Universities for Research in Astronomy, Inc., under NASA contract NAS 5-26555. J.B.H. was supported in part by funding from the NASA Kentucky Space Grant Consortium, Award # 3049024102-11-175. Data used in this study were obtained under programs HST-GO-10864, HST-GO-11336, and HST-GO-12016. We thank A. M. Hughes and S. Andrews for the SMA and Plateau de Bure data. A.B. was supported by the grant HST-GO-11336.01-A, for which observing time was granted by the *Chandra X-ray Observatory* peer review. The authors thank the support staff members of the IRTF telescope for assistance in obtaining the SED data, and the IR&D program at The Aerospace Corporation. We also acknowledge support from NASA NNH06CC28C (M.L.S.) and NNX09AC73G (C.A.G. and M.L.S.). We would like to thank Kenneth Wood and Michael J. Wolff for their quick response to our questions about their dust grain models during private communications. Finally, we thank two anonymous referees for many suggestions that significantly improved this paper. We dedicate this paper to the memory of Bruce Woodgate, a colleague, mentor, and friend who died during the preparation of this paper.

Facility: *HST* (NICMOS, STIS, ACS).

REFERENCES

Adams, F. C., Emerson, J. P., & Fuller, G. A. 1990, ApJ, 357, 606
Agra-Amboage, V., Cabrit, S., Dougados, C., et al. 2014, A&A, 564, A11
Alexander, R. D., Clarke, C. J., & Pringle, J. E. 2006, MNRAS, 369, 229
Andrews, S. M., & Williams, J. P. 2005, ApJ, 631, 1134
Andrews, S. M., Wilner, D. J., Espaillat, C., et al. 2011, ApJ, 732, 42
Ardila, D. R., et al. 2013, ApJS, 207, 1
Banzatti, A., Testi, L., Isella, A., et al. 2011, A&A, 525, A12
Beck, T. L., Bary, J. S., Dutrey, A., et al. 2012, ApJ, 754, 72
Beck, T. L., McGregor, P. J., Takami, M., & Pyo, T.-S. 2008, ApJ, 676, 472
Bertout, C., & Genova, F. 2006, A&A, 460, 499
Bruderer, S., van der Marel, N., van Dishoeck, E. F., & van Kempen, T. A. 2014, A&A, 562, A26
Calvet, N., D'Alessio, P., Watson, D. M., et al. 2005, ApJL, 630, L185
Cardelli, J. A., Clayton, G. C., & Mathis, J. S. 1989, ApJ, 345, 245
Chiang, E. I., Joung, M. K., Creech-Eakman, M. J., et al. 2001, ApJ, 547, 1077
Cieza, L. A., Schreiber, M. R., Romero, G. A., et al. 2012, ApJ, 750, 157
Cotera, A. S., Whitney, B. A., Young, E., et al. 2001, ApJ, 556, 958
Cox, A., Grady, C., Woodgate, B., et al. 2007, BAAS, 38, 199
de Juan Ovelar, M., Min, M., Dominik, C., et al. 2013, A&A, 560, A111
Doering, R. L., Meixner, M., Holfeltz, S. T., et al. 2007, AJ, 133, 2122
Dong, R., Rafikov, R., Zhu, Z., et al. 2012, ApJ, 750, 161
Dullemond, C. P., & Dominik, C. 2005, A&A, 434, 971
Ercolano, B., Clarke, C. J., & Drake, J. J. 2009, ApJ, 699, 1639
Espaillat, C., D'Alessio, P., Hernández, J., et al. 2010, ApJ, 717, 441
Follette, K. B., Tamura, M., Hashimoto, J. & SEEDS Team 2012, in American Astronomical Society Meeting 219 Abstracts, 344.04
France, K., Schindhelm, E., Bergin, E. A., Roueff, E., & Abgrall, H. 2014, ApJ, 784, 127
France, K., Schindhelm, E., Herczeg, G. J., et al. 2012, ApJ, 756, 171
Gianninas, A., Bergeron, P., & Ruiz, M. T. 2011, ApJ, 431, 138
Gilliland, R. L. 1994, ApJL, 435, L63
Gonzaga, S., Biretta, J., et al. 2010, HST WFPC2 Data Handbook (5th edn; Baltimore, MD: STScI)
Gorti, U., & Hollenbach, D. 2009, ApJ, 690, 1539
Grady, C. A., Muto, T., Hashimoto, J., et al. 2013, ApJ, 762, 48
Grady, C. A., Polomski, E. F., Henning, T., et al. 2001, AJ, 122, 3396
Grady, C. A., Schneider, G., Hamaguchi, K., et al. 2007, ApJ, 665, 1391
Gräfe, C., Wolf, S., Roccatagliata, V., Sauter, J., & Ertel, S. 2011, A&A, 533, A89
Güdel, M., Lahuis, F., Briggs, K. R., et al. 2010, A&A, 519, A113
Gullbring, E., Hartmann, L., Briceno, C., & Calvet, N. 1998, ApJ, 492, 323
Hapke, B., Wells, E., Wagner, J., & Partlow, W. 1981, Icarus, 47, 361
Hartigan, P., Edwards, S., & Ghandour, L. 1995, ApJ, 452, 736
Hartigan, P., Hartmann, L., Kenyon, S. J., Strom, S. E., & Skrutskie, M. F. 1990, ApJL, 354, L25
Herczeg, G. J. 2005, PhD thesis, University of Colorado at Boulder, Colorado, USA
Herczeg, G. J., Linsky, J. L., Valenti, J. A., Johns-Krull, C. M., & Wood, B. E. 2002, ApJ, 572, 310
Herczeg, G. J., Linsky, J. L., Walter, F. M., Gahm, G. F., & Johns-Krull, C. M. 2006, ApJS, 165, 256
Herczeg, G. J., Linsky, J. L., Walter, F. M., et al. 2005, AJ, 129, 2777
Hornbeck, J. B., Grady, C. A., Perrin, M. D., et al. 2012, ApJ, 744, 54

Hueso, R., & Guillot, T. 2005, A&A, 442, 703
Hughes, A. M., Andrews, S. M., Espaillat, C., et al. 2009, ApJ, 698, 131
Ingleby, L., Espaillat, C., Calvet, N., et al. 2015, ApJ, 805, 149
Ishihara, D., Onaka, T., Kataza, H., et al. 2010, A&A, 514, A1
Johnstone, D., Hollenbach, D., & Bally, J. 1998, ApJ, 499, 758
Kim, S.-H., Martin, P. G., & Hendry, P. D. 1994, ApJ, 422, 164
Klaassen, P. D., Juhasz, A., Mathews, G. S., et al. 2013, A&A, 555, A73
Koerner, D. W., Sargent, A. I., & Beckwith, S. V. W. 1993, Icarus, 106, 2
Krist, J. E., Stapelfeldt, K. R., Ménard, F., Padgett, D. L., & Burrows, C. J. 2000, ApJ, 538, 793
Landolt, A. U. 1992, ApJ, 104, 340
Lubow, S. H., & D'Angelo, G. 2006, ApJ, 641, 526
Lytle, D., Stobie, E., Ferro, A., & Barg, I. 1999, in ASP Conf. Ser. 172, Astronomical Data Analysis Software and Systems VIII, ed. D. M. Mehringer, R. L. Plante, & D. A. Roberts (San Francisco, CA: ASP), 345
Mathews, G. S., Klaassen, P. D., Juhász, A., et al. 2013, A&A, 557, A132
Mathis, J. S., Rumpl, W., & Nordsieck, K. H. 1977, ApJ, 217, 425
Maybhate, A., & Armstrong, A. 2010, ACS Instrument Handbook (10th edn; Baltimore, MD: STScI)
McMaster, M., Biretta, J., et al. 2008, HST WFPC2 Instrument Handbook (10th edn.; Baltimore, MD: STScI)
Montes, D., López-Santiago, J., Gálvez, M. C., et al. 2001, MNRAS, 328, 45
Muto, T., Grady, C. A., Hashimoto, J., et al. 2012, ApJL, 748, L22
Owen, J. E., Ercolano, B., & Clarke, C. J. 2011, MNRAS, 412, 13
Paardekooper, S.-J., & Mellema, G. 2006, A&A, 453, 1129
Pavlovsky, C., et al. 2006, ACS Data Handbook (5th edn; Baltimore: STScI)
Pérez, L. M., Carpenter, J. M., Chandler, C. J., et al. 2012, ApJL, 760, L17
Pinte, C., Padgett, D. L., Ménard, F., et al. 2008, A&A, 489, 633
Pott, J.-U., Perrin, M. D., Furlan, E., et al. 2010, ApJ, 710, 265
Quillen, A. C., Blackman, E. G., Frank, A., & Varnière, P. 2004, ApJL, 612, L137
Ray, T., Dougados, C., Bacciotti, F., Eislöffel, J., & Chrysostomou, A. 2007, Protostars and Planets V, ed. B. Reipurth, D. Jewitt, & K. Keil (Tucson, AZ: Univ. Arizona Press), 231
Reipurth, B., & Bally, J. 2001, ARA&A, 39, 403
Rice, W. K. M., Armitage, P. J., Wood, K., & Lodato, G. 2006, MNRAS, 373, 1619
Robitaille, T. P., Whitney, B. A., Indebetouw, R., & Wood, K. 2007, ApJS, 169, 328
Salyk, C., Blake, G. A., Boogert, A. C. A., & Brown, J. M. 2011, ApJ, 743, 112
Salyk, C., Herczeg, G. J., Brown, J. M., et al. 2013, ApJ, 769, 21
Saucedo, J., Calvet, N., Hartmann, L., & Raymond, J. 2003, ApJ, 591, 275
Schneider, G., & Stobie, E. 2002, in Astronomical Data Analysis Software and Systems XI, ed. D. A. Bohlender, D. Durand, & T. H. Handley (San Francisco, CA: ASP), 382
Schneider, G., Wood, K., Silverstone, M. D., et al. 2003, AJ, 125, 1467
Schneider, P. C., Eislöffel, J., Güdel, M., et al. 2013, A&A, 550, L1
Seale, J. P., & Looney, L. W. 2008, ApJ, 675, 427
Simon, M., & Prato, L. 1995, ApJ, 450, 824
Stapelfeldt, K., Burrows, C. J., Koerner, D., et al. 1995, The WFPC2 IDT, in BAAS, Vol. 27, 1446
Stark, D. P., Whitney, B. A., Stassun, K., & Wood, K. 2006, ApJ, 649, 900
Strassmeier, K. G. 2009, A&ARv, 17, 251
Walter, F. M., Brown, A., Linsky, J. L., et al. 1987, ApJ, 314, 297
Walter, F. M., Herczeg, G., Brown, A., et al. 2003, AJ, 126, 3076
Watson, A. M., & Stapelfeldt, K. R. 2007, AJ, 133, 845
Weintraub, D. A., Sandell, G., & Duncan, W. D. 1989, ApJL, 340, L69
White, R. J., & Ghez, A. M. 2001, ApJ, 556, 265
Whitney, B. A., & Hartmann, L. 1992, ApJ, 395, 529
Whitney, B. A., Robitaille, T. P., Bjorkman, J. E., et al. 2013, ApJS, 207, 30
Whittet, D. C. B., Gerakines, P. A., Hough, J. H., & Shenoy, S. S. 2001, ApJ, 547, 872
Wisniewski, J. P., Clampin, M., Grady, C. A., et al. 2008, ApJ, 682, 548
Wolk, S. J., & Walter, F. M. 1996, AJ, 111, 2066
Wood, K., Lada, C. J., Bjorkman, J. E., et al. 2002a, ApJ, 567, 1183
Wood, K., Wolff, M. J., Bjorkman, J. E., & Whitney, B. 2002b, ApJ, 564, 887
Zhu, Z., Nelson, R. P., Dong, R., Espaillat, C., & Hartmann, L. 2012, ApJ, 755, 6